A fully Lagrangian formulation for fluid-structure interaction problems with free-surface fluids and fracturing solids

Alejandro Cornejo · Alessandro Franci · Francisco Zárate · Eugenio Oñate

Received: date / Accepted: date

Abstract This paper presents a novel coupled formulation for fluid-structure interaction (FSI) problems involving free-surface fluid flows, fracture phenomena, solid mutual contact and large displacements. The numerical formulation combines three different Lagrangian computational methods. The Particle Finite Element Method (PFEM) is used to solve the free-surface fluid flow, a Finite Element Method (FEM) with smoothed isotropic damage model is employed for the solution of solid structures and debris, finally, the Discrete Element Method (DEM) is used to manage the contact interaction between different solid boundaries, including the new ones generated by propagating cracks. The proposed method has a high potential for the prediction of the structural damages on civil constructions caused natural hazards, such as floods, tsunami waves or landslides. Its application field can also be extended to fracture phenomena in structures and soils/rocks arising from explosions or hydraulic fracking processes. Several numerical examples are presented to show the validity and accuracy of the numerical technique proposed.

Keywords Fracture Mechanics · Free-Surface Flow · Fluid-Structure Interaction · Discrete Element Method · Particle Finite Element Method

1 Introduction

This work presents a new coupled numerical method for the simulation of structures collapsing and fracturing under the impact of free-surface fluids. This type of FSI problems is of high interest for different engineering applica-

Alejandro Cornejo Velázquez
International Centre for Numerical Methods in Engineering
Carrer del Gran Capità, S/N, 08034 Barcelona
Tel.: +34 934 01 74 95
E-mail: acornejo@cimne.upc.edu

tions, such as in the case of civil infrastructures affected by natural hazards, like floods, tsunami waves or landslides.

The numerical simulation of these multi-coupled problems is challenging due to their high non-linearity and the complexity of the involved phenomena. Indeed, the numerical method must be able to deal with free-surface fluids undergoing large changes of topology and interacting with structures that can break and desegregate into smaller solid debris which, in turn, may eventually hit other structures.

The complexity of this scenario explains the reduced number of computational methods for FSI problems with fracture phenomena available in the literature. Most of these works are focused on the structural failure of pipes and vessels subjected to shocks and explosions [52,50,49,51,47,48,53]. Another important research area in this field refers to the simulation of hydraulic fracture processes, see [56,57,59,58]. On the other hand, a smaller number of works analyzed the collapse of civil structures caused by the impact of free-surface fluid flows, which is the main focus of the present work. In [55], a FSI formulation with a phase-field fracture model was proposed for the structural failure caused by the impact of fluid flows in closed domains. In [54], similar problems were analyzed considering also the fragmentation of the structure due to the cracks propagation. In [62], free-surface fluids were also considered using a coupled Smoothed Particle Hydrodynamics - Discrete Element Method (SPH-DEM) model. Other SPH-based works analyzed the effect of tsunami waves on civil infrastructures, especially bridges, although fracture phenomena were not taken into account [44,43,42]. Still in this research line, it is worth to mention the following coupled methods based on SPH [61], Immersed Particle Method (IBM) [63,64] and DEM-LBM (Lattice Boltzman Method) [65].

The Particle Finite Element Method (PFEM) [38] also been used to model similar fluid-solid interaction, such as in [19,7], but without modeling fracture phenomena. On the other hand, in the coupled PFEM-DEM model proposed in [45,46] for bed erosion processes in river dynamics, the river bed domain was allowed to suffer changes of topology due to the erosion induced by the fluid flow. However, the detached parts could be modeled either as a set of dimensionless DEM particles or as rigid bodies, and not as deformable solids capable of fracturing again, as it is done in the present work.

The FSI problem is here solved with a novel hybrid strategy that combines three different Lagrangian numerical methods. The free-surface flow problem is solved with the stabilized PFEM formulation presented in [7], while the solid deformation, fracture and frictional contact effect are modeled by combining a Finite Element Method (FEM) with smoothed isotropic damage model [3,16] and a Discrete Element Method (DEM) [13–15], in the spirit of the so-called FEM-DEM procedure [1–3].

In the specific type of FSI problems considered in this work, the solution accuracy strictly depends on the capability of the numerical method to track the evolving fluid-solid interface. This task is particularly critical for the problems analyzed here because, on the one hand, the fluids have a free surface which

changes continuously during the analysis and, on the other hand, the solids can undergo large displacements/rotations and their contours can change significantly due to the propagating cracks and the resulting fragmentation of the structure. In this work, the fluid-solid interface is detected automatically with the PFEM during its remeshing step. Remarkably, the remeshing procedure used in the PFEM not only improves the quality of the finite element discretization and defines the updated fluid free surface, but also allows to detect the new contact surfaces with the solid bodies. The Lagrangian nature of the PFEM guarantees also that all the nodes of the interface belong to both the fluid and the solid meshes. This allows us to avoid projecting nodal variables between the solid and the fluid domains. In this sense, the coupled approach here proposed can be classified as a body-fitted conforming-mesh FSI method [27]. Compared to mesh-free [29], non-conforming mesh [28,30] and embedded [37] FSI approaches, body-fitted algorithms allow for an easier transmission of boundary conditions between fluid and solid domains. Nevertheless, these methods generally require a similar size of fluid and solid elements at the interface zone and may lead to mesh distortion issues when applied to large deformation problems. For large and arbitrary motions of the interface, this latter task can become critical for conforming-mesh methods based on Arbitrary Lagrangian-Eulerian (ALE) techniques [35]. Conversely, the PFEM can naturally track the evolving interface and, at the same time, maintains a good discretization, also in the presence of large and unpredictable motion of the fluid-solid interface. This feature represents one of the main advantages of the PFEM for coupled fluid-solid mechanics analysis and also explains the extended use of the method for FSI problems [34,20,31,6,32,33,5].

Once the contact interfaces between fluids and solids have been detected, the FSI time step solution is performed through a Aitken iterative scheme [60]. A staggered method has been preferred to a monolithic one to avoid the ill-conditioning of the linear system which could arise due to different orders of magnitude of the physical parameters of the materials. This situation is prone to occur in the problems of interest of this work which involves civil structures that are generally characterized by a high stiffness.

Concerning the solid mechanics solution scheme, the FEM-DEM approach chosen can be classified as a hybrid continuum-discrete formulation for fracture mechanics. The onset of cracking is detected using a continuum FEM formulation and an isotropic damage model [16]. On the other hand, the DEM is used to compute the repulsion forces due to the contact interaction between different solid contours, including those of propagating cracks. Before fracturing, the stiffness degradation of the material and the crack initialization are modelled in a smeared way. During this phase, the mesh topology is not changed and the fracture is represented by stress softening and localization. When the inelastic energy dissipation reaches the fracture energy in some zones of the solid, the finite elements contained therein are removed from the mesh and replaced by a mass-equivalent set of particles, or discrete elements. A substepping procedure is employed in the time marching scheme to synchronize the FEM implicit solution and the DEM explicit one.

One of the main advantages of the FEM-DEM methodology lays in its capability to model in a natural way the onset, evolution, merging and branching of fractures, as well as the eventual detachment of solid blocks, their mutual contact, and their independent motion under the effect of the fluid flow. This feature is particularly important for the problems of interest for this work, because loose solid debris may be at the origin of other damages on structures or living beings.

The paper has been structured as follows. In Section 2, the governing equations for the solid and the fracture model are presented. In Section 3, the fluid governing equations and the PFEM scheme is presented. In Section 4, the FSI solution algorithm through the proposed PFEM-FEM-DEM approach is described. In Section 5, several numerical examples are analyzed to validate the overall methodology. Finally, the concluding remarks of the work are presented in Section 6.

2 Solid mechanics problem

The solid parts of the domain are solved with a coupled FEM-DEM approach [1–3]. This method combines a continuum FEM formulation with the DEM to simulate fracturing solids and the consequent formation of solid debris. In this section, we first present the governing equations and the FEM solution scheme, then we describe the damage and fracture models, and finally the FEM-DEM algorithm to deal with crack propagation and frictional contact between the interacting solids.

2.1 Governing equations for the solid

The solid motion is governed by the linear momentum equations formulated in a Total Lagrangian (TL) framework as

$$\rho_s \ddot{\mathbf{u}} - \mathrm{Div}\mathbf{P} - \mathbf{b}_0 = \mathbf{0} \text{ in } \Omega_{s0} \times [0, T] \tag{1}$$

where ρ_s is the solid density, $\mathbf{u}$ is the displacement field, $\mathbf{P}$ is the first Piola-Kirchhoff stress tensor, $\mathbf{b}_0$ is the external body force per current unit volume over the undeformed solid configuration Ω_{s0}, and T is the total time duration.

A set of initial conditions specifying displacements at time $t = 0$ are defined as:

$$\mathbf{u}(t = 0) = \hat{\mathbf{u}}_0 \text{ in } \Omega_0 \tag{2}$$

$$\mathbf{v}(t = 0) = \hat{\mathbf{v}}_0 \text{ in } \Omega_0 \tag{3}$$

where $\mathbf{v}$ are the velocities, and $\hat{\mathbf{u}}_0$ and $\hat{\mathbf{v}}_0$ are the initial displacements and velocities, respectively.

The governing equations set is closed by the following boundary conditions

$$\mathbf{P} \cdot \mathbf{N} = \hat{\mathbf{t}}_0 \ \text{ in } \ \Gamma_\sigma \times [0, T] \tag{4}$$

$$\mathbf{u} = \hat{\mathbf{u}} \ \text{ in } \ \Gamma_u \times [0, T] \tag{5}$$

where $\mathbf{N}$ is the unit normal vector, $\hat{\mathbf{t}}_0$ are the tractions applied on the Neumann boundary Γ_σ, and $\hat{\mathbf{u}}$ are the prescribed displacements to the Dirichlet contours Γ_u.

In this coupled approach, the traction vector $\hat{\mathbf{t}}_0$ is computed as the sum of three different contributions as

$$\hat{\mathbf{t}}_0 = \mathbf{t}_{\text{loads}} + \mathbf{t}_{\text{contact}} + \mathbf{t}_{\text{fluid}} \tag{6}$$

where $\mathbf{t}_{loads}$ are the tractions arising from standard external loads, $\mathbf{t}_{contact}$ are the tractions due to the contact with other solid bodies, and $\mathbf{t}_{fluid}$ are the tractions induced by the fluid pressures.

2.1.1 Finite element solution

The solid governing equations (Eq. (1)) are solved with an implicit scheme, using 3-nodded triangular elements in 2D and 4-nodded tetrahedral in 3D. Each time step is solved iteratively for the increments of nodal displacements $\Delta\bar{\mathbf{u}}$ (the upper bar $\bar{\cdot}$ denotes a nodal variable). The derivation of the fully discretized and linearized form of the governing equations is considered out of the scope of the present work. Interested readers may refer to [1–3] for details. For a generic time step $\left[{}^{n}t; {}^{n+1}t\right]$ of duration Δt, the following linear system is solved for each iteration k:

$$\mathbf{K}(\bar{\mathbf{u}}_k) \cdot \Delta\bar{\mathbf{u}}_{k+1} = -\mathbf{r}(\bar{\mathbf{u}}_k). \tag{7}$$

being:

$$\mathbf{r}(\bar{\mathbf{u}}_k) = \mathbf{M}\,\bar{\mathbf{a}}_k + \mathbf{C}\,\bar{\mathbf{v}}_k + \mathbf{f}_{\text{int}}(\bar{\mathbf{u}}_k) - {}^{n+1}\mathbf{f}_{\text{ext}} - {}^{n+1}\mathbf{f}_{\text{fluid}} - {}^{n}\mathbf{f}_{\text{contact}} \tag{8}$$

and

$$\mathbf{K}(\bar{\mathbf{u}}_k) = \left[\frac{1}{\beta\Delta t^2}\mathbf{M} + \frac{\gamma}{\beta\Delta t}\mathbf{C} + \mathbf{K}_T(\bar{\mathbf{u}}_k)\right]. \tag{9}$$

where $\bar{\mathbf{a}}_k$ are the nodal accelerations computed at the k^{th} iteration, $\mathbf{f}_{\text{int}}$ and $\mathbf{f}_{\text{ext}}$ are the internal and external forces vectors, respectively, $\mathbf{f}_{\text{fluid}}$ are the equivalent nodal forces due to the fluid pressure, $\mathbf{f}_{\text{contact}}$ are the equivalent contact nodal forces, which are here evaluated at ${}^{n}t$, $\mathbf{M}$, $\mathbf{C}$ and $\mathbf{K}_T$ are the mass, damping and tangential stiffness matrices, respectively, and the parameters $\beta = 0.25$, $\gamma = 0.5$ have been used.

For the sake of completeness, all the variables and matrices introduced in Eqs.(8-9) are defined in Appendix A.

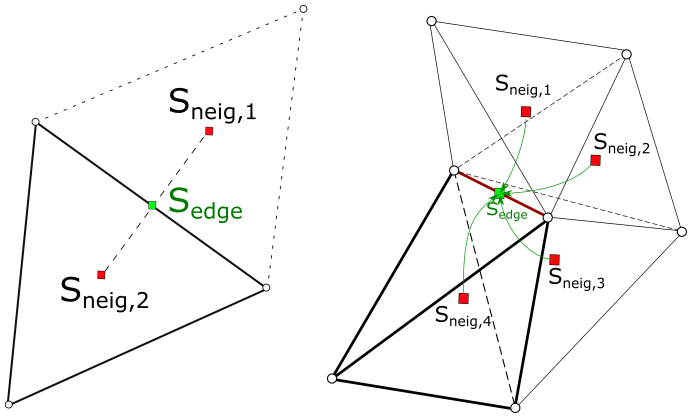

(a) 2D (b) 3D

Fig. 1: *Super-convergent* points. Graphical representation of the effective stress smoothing at the FE edge.

2.2 Damage and fracture models

For the fracture analysis, the isotropic damage model proposed by Oliver et al. [16] for crack propagation in concrete has been used. In this model, the internal damage variable d describes the material degradation, varying from 0 (intact material) to 1 (fully damaged material). The constitutive model relates the Green-Lagrange strain tensor $\mathbf{E}$ with the second Piola-Kirchhoff stress tensor $\mathbf{S}$ as:

$$\mathbf{S} = \boldsymbol{\mathcal{C}}_s \, \mathbf{E} = (1-d) \, \boldsymbol{\mathcal{C}}_0 \, \mathbf{E} = (1-d) \, \hat{\mathbf{S}}, \tag{10}$$

where $\hat{\mathbf{S}}$ is the effective second Piola-Kirchhoff stress tensor, $\boldsymbol{\mathcal{C}}_s = (1-d)\,\boldsymbol{\mathcal{C}}_0$ is the secant constitutive tensor, and $\boldsymbol{\mathcal{C}}_0$ the elastic constitutive tensor.

The damage parameter d is computed by evaluating the effective stresses at the mid-sides of the adjacent elements. This allows us to obtain super-convergence values of the stresses at these points [25,26]. This means that the error of the computed values at these points decreases with a higher rate of convergence.

Fig. 1 shows the scheme to compute the effective stress tensor $\hat{\mathbf{S}}$ at the edges from the stress tensors evaluated at the integration points of the finite elements sharing that edge as:

$$\hat{\mathbf{S}}^{\text{edge}} = \frac{1}{n_{elem}} \sum_{i=1}^{n_{elem}} \hat{\mathbf{S}}^{\text{neig,i}} \tag{11}$$

where n_{elem} is the number of elements sharing the edge.

The effective stress tensor at each element edge is also used to evaluate whether the material is in elastic or inelastic regime basing on the following general definition of yield surface Φ

$$\Phi = f(\hat{\mathbf{S}}^{\text{edge}}) - \sigma^{\tau,\text{edge}} \leq 0 \tag{12}$$

where $f(\hat{\mathbf{S}}_{edge})$ is the so-called equivalent effective stress whose definition depends on the yield surface of interest and $\sigma_{\tau}^{\text{edge}}$ is the stress threshold which is computed as:

$$\sigma^{\tau,\text{edge}} = \max(\sigma^{\tau_0}, \max(f(\hat{\mathbf{S}}^{\text{edge}})_t)) \; t \in [0,T], \tag{13}$$

where σ^{τ_0} is the initial yield strength of the material.

This definition guarantees that the material threshold is the maximum historical equivalent stress achieved and also ensures the irreversibility of the damaging process.

The internal damage variable d is also evaluated at each edge of the elements using the following exponential softening law:

$$d(\hat{\mathbf{S}}^{\text{edge}}) = 1 - \frac{\sigma^{\tau_0}}{f(\hat{\mathbf{S}}^{\text{edge}})} \exp\left(A\left(1 - \frac{f(\hat{\mathbf{S}}^{\text{edge}})}{\sigma^{\tau_0}}\right)\right) \tag{14}$$

in which the parameter A is determined from the energy dissipated in a uniaxial tension test as [16]

$$A = \left(\frac{G_f E}{\hat{l}(\sigma^{\tau_0})^2} - \frac{1}{2}\right)^{-1} \tag{15}$$

being G_f is the specific fracture energy per unit area (taken as a material property), E is the Young modulus, $\hat{l}$ is the characteristic length of the element, and σ^{τ_0} is the initial tensile yield strength.

The elemental damage is computed after evaluating the damage variables at all its edges and all the possible fracture modes, like those represented in Fig. 2. In 2D, the elemental damage will be always the mean value of the two highest damage variables of the three edges of the element, thus:

$$d_{elem} = \frac{1}{2}\left(d_{\text{edge,max}} + d_{\text{edge,max}-1}\right) \tag{16}$$

If the damage computed at a certain finite element becomes higher than a pre-fixed threshold (≈ 0.98), this element is removed from the FE mesh and a set of DE is placed over the nodes of the erased FE [1–3]. As it will be explained below, these DE are used to compute the contact forces between different solids, or between different parts of the same structure.

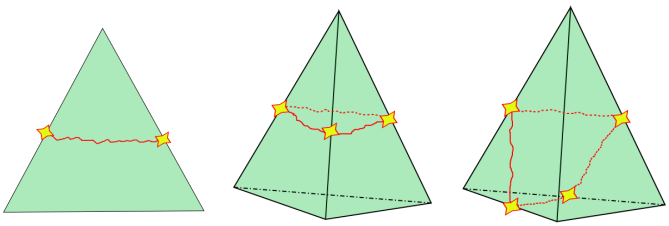

(a) 2D version (b) 3 Edged mode (c) 4 Edged mode

Fig. 2: Different fracture modes in 2D and 3D element geometries [3].

2.3 Contact forces computation with the DEM

In order to prevent the inter penetration of solid elements faces, a set of discrete elements is overlapped to the boundary nodes of the solid. In the case of a propagating fracture, additional discrete elements are placed over the new boundary nodes of the crack. Once a DE detects an active contact with another solid boundary, either with another DE or a FE edge, a repulsive force is computed and transmitted to the FEM nodes.

The DEM procedure used within the FEM-DEM formulation is based on the works of Casas et al [17], Oñate et al [13] and Thornton et al. [18].

Considering two colliding particles, whose coordinates are $\mathbf{r_1}$ and $\mathbf{r_2}$, the normal vector that aligns the centres of the spheres is computed as follows:

$$\mathbf{n_{21}} = \frac{\mathbf{r_2} - \mathbf{r_1}}{\|\mathbf{r_2} - \boldsymbol{r_1}\|} \ , \ \mathbf{n_{21}} = -\mathbf{n_{12}}. \tag{17}$$

The normal indentation δ_n between the discrete particles is computed as:

$$\delta_n = R_1 + R_2 - \|\mathbf{r_{21}}\| \ \ , \ \mathbf{r_{21}} = \mathbf{r_2} - \mathbf{r_1}. \tag{18}$$

where R_i is the radius of particle i.

The total contact force between two particles $\mathbf{F}_{contact}$ is decomposed into its normal and tangential components as:

$$\mathbf{F}_{contact} = F_n \, \mathbf{n} + F_t \, \mathbf{t} \tag{19}$$

The normal component of the contact force F_n is obtained as a combination of an elastic ($F_{n,el}$) and a viscous ($F_{n,damp}$) contribution, *i.e.*:

$$F_n = F_{n,el} + F_{n,damp} \tag{20}$$

Considering a standard Hertzian model, the elastic part is computed as:

$$F_{n,el} = \frac{4}{3} \tilde{R}^{\frac{1}{2}} \tilde{E} \delta_n^{\frac{3}{2}} \tag{21}$$

where $\tilde{R} := (1/R_1 + 1/R_2)^{-1}$, $\tilde{E} = \left(1/\tilde{E}_1 + 1/\tilde{E}_2\right)^{-1}$ with $\tilde{E}_i := E_i/(1 - \nu_i^2)$, being ν_i the Poisson ratio, E the Young modulus and R the radius of each particle.

The viscous damping contribution is computed as:

$$F_{n,damp} = c_n \, \delta_n^{1/4} \, \dot{\delta_n}. \tag{22}$$

For particle-particle contact the constant c_n is given by

$$c_n = \gamma \sqrt{8 \, \tilde{E} \, \tilde{M} \sqrt{\tilde{R}}} \tag{23}$$

being $\tilde{M} := (1/m_1 + 1/m_2)^{-1}$ and γ a viscous damping coefficient.

On the other hand, the tangential component of the contact force (Eq. 19) is computed as:

$$\mathbf{F_t} = F_{t,el} \, \mathbf{t}_d + F_{t,damp} \mathbf{t}_\nu \tag{24}$$

where the directions $\mathbf{t_d}$ and $\mathbf{t}_\nu$ are based on the kinematics during tangential deformation [13].

The elastic tangential contribution is obtained by:

$$F_{t,el} = \delta_n^{1/2} \int 8G\dot{\delta} \, dt \tag{25}$$

being G the shear modulus. The tangential viscous contribution as

$$F_{t,damp} = c_t \, \delta_n^{1/4} \dot{\delta_t} \tag{26}$$

with

$$c_t = 2 \, \gamma \sqrt{8 \, \tilde{G} \, \tilde{M} \, \sqrt{\tilde{R}}} \tag{27}$$

where $\tilde{G} = G/(4 - 2\nu)$ and $G = E/(2 + 2\nu)$.

2.4 FEM-DEM solution scheme

As the FEM solution is obtained via an implicit scheme and the DEM with an explicit one, the time step increment used in the two methods may be of different orders of magnitude. Thus, to optimize the computational performance of the method, a sub-stepping procedure is used. Thus, for each time step increment of the FEM solution (Δt), the DEM problem is solved several times using a smaller time increment (Δt_e). Note that the time step used for the FEM solid solution is the same as the one used for the implicit PFEM solution of the fluid parts of the domain.

The iterative FEM solution (Eqs.(7)-(9)) is obtained considering the contact forces computed at the end of the previous time step. Once the numerical solution of the solid has converged, the kinematic information of the FEM boundary nodes is transferred to the respective discrete element. In case of having an active solid-solid interaction, the kinematic information is used to

compute the new contact forces through a sub-stepping loop. At each explicit time step (^{e}t), the kinematic information of each particle is updated by interpolating the FEM results obtained at the previous time step (^{n}t) and those of the converged one (^{n+1}t). This information is used to compute the corresponding contact force contribution $\mathbf{F}_{contact}$ from Eq.(19), which is added to the accumulated impulse $\mathbf{I}(^{e}t)$ as

$$\mathbf{I}(^{e}t) = \mathbf{I}(^{e-1}t) + \Delta t_e \cdot \mathbf{F}_{contact} \tag{28}$$

Once the sub-stepping is finalized ($^{e}t = {}^{n+1}t$), the contact forces needed in the FEM solution of the following time step (Eq.8) are computed as

$$\mathbf{f}_{contact} = \frac{\mathbf{I}(^{e}t)}{\Delta t} \tag{29}$$

Algorithm 1 summarizes the solution scheme of the FEM-DEM method.

3 Fluid dynamics problem

3.1 Governing equations of the fluid

The governing equations for the fluid dynamics problem are the linear momentum balance and the mass conservation equations. The problem is solved in an Updated Lagrangian framework as in the standard PFEM [19]. Calling Ω_f the updated fluid domain, the fluid governing equations read

$$\rho_f \frac{\partial \mathbf{v}}{\partial t} - \bigtriangledown \cdot \boldsymbol{\sigma} - \rho_f \mathbf{g} = \mathbf{0} \qquad \text{in } \ \Omega_f \times (0,T) \tag{30}$$

$$\bigtriangledown \cdot \mathbf{v} - \frac{1}{\kappa_f}\frac{\partial p}{\partial t} = 0 \qquad \text{in } \ \Omega_f \times (0,T) \tag{31}$$

where $\mathbf{v}$ is the velocity vector, t is the time, $\boldsymbol{\sigma}$ is the fluid Cauchy stress tensor, $\mathbf{g}$ is the gravity acceleration vector, and ρ_f and κ_f are the fluid density and bulk modulus, respectively.

For Newtonian fluids, the Cauchy stress tensor is splited as

$$\boldsymbol{\sigma} = p\mathbf{I} + 2\,\mu_f\,\mathbf{d'} \tag{32}$$

where p is the pressure, $\mathbf{I}$ is the 2^{nd} order identity tensor, μ_f is the fluid dynamic viscosity, and $\mathbf{d'}$ is the deviatoric part of the deformation rate tensor $\mathbf{d}$ computed as

$$\mathbf{d'} = \frac{1}{2}\left(\bigtriangledown \mathbf{v} + (\bigtriangledown \mathbf{v})^T\right) - \frac{1}{3} d_v \mathbf{I} \tag{33}$$

where $d_v = \bigtriangledown \cdot \mathbf{v}$ is the volumetric deformation rate.

Following [20,21,10], the mass conservation equation (Eq.(31)) is here solved not in the standard divergence-free form of the Navier-Stokes problem ($\bigtriangledown \cdot \mathbf{v} = 0$), but considering a certain (small) compressibility of fluid

Algorithm 1: FEM-DEM solution algorithm for a generic time step $\left[{}^{n}t; {}^{n+1}t\right]$ of duration Δt.

Initialization of the implicit transient dynamic scheme for the FEM:
$k \leftarrow 0$, $\bar{\mathbf{u}}_0 \leftarrow {}^{n}\bar{\mathbf{u}}$
Apply the DE contact forces obtained at the last time step as equivalent nodal force for the FEM (${}^{n}\mathbf{f}_{contact}$ of Eq.8)
while $\left\|\boldsymbol{r}_{\text{eff,dyn}}\right\| > tol$ **do**
  for *Elements* **do**
    Compute the effective stresses $\bar{\boldsymbol{\sigma}} = \mathbf{C_0} : \boldsymbol{\varepsilon}$
    Smoothing of the effective stress field at the FE edges
    Compute the damage d at the edges by Eq. (14)
    Obtain the elemental damage by Eq. (16)
    Calculate the elemental tangent stiffness matrix $\mathbf{K}_T^{(e)}$ and internal forces vector $\mathbf{f}_{\text{int}}^{(e)}$
    Assemble elemental contributions: $\mathbf{K}_T \leftarrow \mathbf{K}_T^{(e)}$ and $\mathbf{f}_{\text{int}} \leftarrow \mathbf{f}_{\text{int}}^{(e)}$
  end
  Calculate the displacement increments $\Delta\mathbf{u}_{k+1} = \mathbf{K}_T^{-1}\mathbf{r}_k$
  k += 1
end
for *Elements* **do**
  if *Damage* $\geq$ *0.98* **then**
    Erase the FE
    Generate the Discrete Elements (DE) at the nodes of the damaged FE
  end
end
Initialization of the explicit transient dynamic scheme for the DEM
${}^{e}t \leftarrow {}^{n}t$
while ${}^{e}t \leq {}^{n+1}t$ **do**
  ${}^{e}t$ += Δt_e
  Obtain the FEM kinematic information for the DE by interpolating the FEM results between the initial time (${}^{n}t$) and the final one (${}^{n+1}t$)
  Compute the contact forces $\mathbf{F}_{contact}$ using Eq. (19)
  Update the explicit contact impulses at each particle using Eq. (28)
  Integrate the equations of motion for the free particles
  Compute the displacements, velocities, and accelerations of free particles
end
Compute the updated equivalent contact nodal forces ${}^{n+1}\mathbf{f}_{contact}$ using Eq. (29)

material. For values of bulk modulus going to infinity the divergence-free form of the continuity equation is recovered.

The fluid governing equations are completed by the following boundary conditions at the Dirichlet (Γ_f^v) and Neumann (Γ_f^t) boundaries

$$\begin{aligned} \mathbf{v} &= \hat{\mathbf{v}} \qquad && \text{on } \Gamma_f^v \\ \boldsymbol{\sigma} \cdot \mathbf{n} &= \hat{\mathbf{t}} \qquad && \text{on } \Gamma_f^t \end{aligned} \tag{34}$$

being $\mathbf{n}$ the normal vector to the fluid boundaries, $\hat{\mathbf{v}}$ the prescribed velocities at the Dirichlet boundaries and $\hat{\mathbf{t}}$ the prescribed tractions at the Neumann ones.

3.2 Finite element solution

The fluid governing equations are solved in a standard FEM fashion following the implicit stabilized velocity-pressure strategy presented in [9]. The domain is discretized with simplicial elements (triangles in 2D and tetrahedra in 3D) using linear shape functions for both the velocity and pressure fields. The formulation is stabilized with the Finite Increment Calculus (FIC) technique [22, 9, 23]. In the FIC scheme for Lagrangian formulations [9], the stabilization terms are added to the continuity equation only. The derivation of the FIC-FEM stabilized form of the fluid governing equations is considered out of the scope of this work. Details can be found in [9]. In this section, only the final fully-discretized and linearized form is given.

The time step solution is obtained through an iterative two-step procedure where the linear momentum equations are solved for the increments of nodal velocities $\Delta\bar{\mathbf{v}}$ and the stabilized continuity equation is solved for the nodal pressures $\bar{\boldsymbol{p}}$.

Considering a generic time step $\left[{}^{n}t;{}^{n+1}t\right]$ of duration Δt (same time step used for the FEM solution of the solid mechanics problem), at each iteration k, the increment of nodal velocities are obtained from the discretized form of the linear momentum equations (Eq. (30)) as

$$\left(\mathbf{K}^{\rho}+\mathbf{K}^{m}\right)\boldsymbol{\Delta}\bar{\mathbf{v}}_{k+1}=\mathbf{r}_{k} \tag{35}$$

with

$$\begin{aligned}
&\mathbf{K}^{\rho}_{IJ}=\mathbf{I}\int_{\Omega}\frac{2\rho_f}{\Delta t}N_I N_J d\Omega, \quad \mathbf{K}^{m}_{IJ}=\int_{\Omega}\mathbf{B}^{T}_{I}\mathbf{C}\mathbf{B}_J d\Omega \\
&r_{Ii}=\int_{\Omega}\rho_f N_I N_J d\Omega\;\bar{\dot{v}}_{Ji}+\int_{\Omega}\frac{\partial N_I}{\partial x_j}\sigma_{ij}d\Omega-\int_{\Omega}\rho_f g_i N_I d\Omega
\end{aligned} \tag{36}$$

where N_I is the linear shape functions for node I and matrices $\mathbf{B}$ and $\mathbf{C}$ are defined for a two dimensional problem as follows

$$\mathbf{B}_I=\begin{bmatrix}\dfrac{\partial N_I}{\partial x} & 0\\ 0 & \dfrac{\partial N_I}{\partial y}\\ \dfrac{\partial N_I}{\partial y} & \dfrac{\partial N_I}{\partial x}\end{bmatrix},\quad \mathbf{C}=\begin{bmatrix}\hat{\kappa_f}\Delta t+\dfrac{4\mu_f}{3} & \hat{\kappa_f}\Delta t-\dfrac{2\mu_f}{3} & 0\\ \hat{\kappa_f}\Delta t-\dfrac{2\mu_f}{3} & \hat{\kappa_f}\Delta t+\dfrac{4\mu_f}{3} & 0\\ 0 & 0 & \mu_f\end{bmatrix} \tag{37}$$

The pseudo-bulk modulus $\hat{\kappa_f}$ used in the fluid constitutive matrix $\boldsymbol{C}$ is obtained by reducing *ad hoc* the real fluid bulk modulus κ_f to avoid ill-conditioning the algebraic linear system [10].

After solving solution of Eq. (35) and updating the fluid kinematic with the new velocities, the fluid nodal pressures $\bar{\boldsymbol{p}}$ are computed from the discretized FIC-stabilized form of the continuity equation (Eq. (31)) as follows

$$\left(\mathbf{M}+\mathbf{S}^{\tau}\right)\bar{\mathbf{p}}_{k+1}=\mathbf{M}^{n}\bar{\mathbf{p}}-\mathbf{Q}^{T}\bar{\mathbf{v}}_{k+1}+\mathbf{f}^{\tau}_{k+1} \tag{38}$$

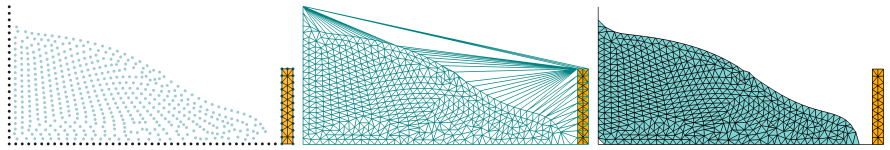

(a) Erase elements (b) Delaunay triangulation (c) Alpha Shape method

Fig. 3: PFEM remeshing steps. Not active fluid-structure interaction.

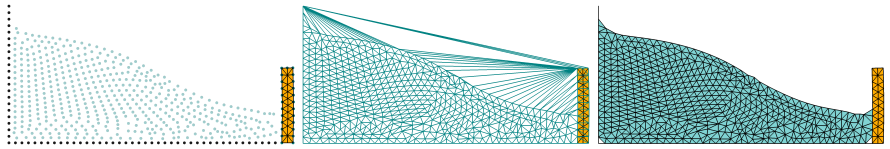

(a) Erase elements (b) Delaunay triangulation (c) Alpha Shape method

Fig. 4: PFEM remeshing steps. Active fluid-structure interaction.

with

$$M_{IJ} = \int_\Omega \frac{N_I N_J}{\kappa_f \Delta t} d\Omega, \quad \mathbf{Q}_{IJ} = \int_\Omega \mathbf{B}_I^T \mathbf{m} N_J d\Omega \tag{39}$$

where, for two dimensional problems, $\mathbf{m} = [1, 1, 0]^T$.

$\mathbf{S}^\tau$ and $\mathbf{f}^\tau$ are the stabilizing terms arising from the FIC method [9] and are given in Appendix B.

Eq.(35) and Eq.(38) are solved iteratively within each fluid time step increment until the fulfillment of the convergence criterion chosen.

3.3 Remeshing procedure with the PFEM

The fluid governing equations are solved using a Lagrangian mesh. For fluid dynamics problems, this strategy leads inevitably to a deterioration of the mesh quality. This inconvenience is circumvented in the PFEM by building a new discretization from the nodes of the previous mesh, whenever this mesh has exceeded a threshold level of distortion. The remeshing step of the PFEM is done by combining Delaunay triangulation [12] and the Alpha Shape method [11]. Figs. 3 and 4 show graphically the PFEM remeshing steps for two different situations of FSI analysis. In particular, Fig. 3 shows a time instant in which the fluid and the solid domains are not interacting, whereas Fig. 4 represents a situation in which the fluid-solid interaction is active.

As shown in Figs. 3a and 4a, the first step of PFEM remeshing consists of erasing all the fluid elements of the previous distorted mesh. It is important to note that the nodes of the previous mesh are preserved together with all the problem information (nodal unknowns and physical parameters) and the solid mesh is not affected by the PFEM remeshing.

In the second step of remeshing, the Delaunay triangulation is built over the cloud of points formed by the nodes of the previous mesh. As shown in Figs. 3b and 4b, the Delaunay mesh is built also considering the nodes belonging to rigid contours and the boundary nodes of the solid domain (interface nodes).

In order to recognize the actual boundaries of the fluid domain (both the free surface and the new interface with the solid and rigid boundaries), the Alpha Shape method is applied. This technique evaluates the quality of all the elements created by the Delaunay triangulation and removes from the mesh those elements that exceed a limit value of distortion or size. In this way, the algorithm is capable to recognize the updated boundaries of the computational domain with good accuracy, as shown in Fig. 3c and 4c. This step is crucial to establish whether the fluid and the solid domains are in contact or not. In the positive case, the fluid and the solid solutions will be coupled, as in the situation described in Fig. 4. In the opposite case (Fig. 3), the fluid solution will not be affected by the solid one and vice versa, at least for the duration of the next time step increment.

More details about the PFEM remeshing process and its implications can be found in [24, 7, 8].

The overall PFEM solution scheme for a generic time step $\left[{}^{n}t; {}^{n+1}t\right]$ of duration Δt is summarized in Algorithm 2.

Algorithm 2: PFEM solution algorithm for free-surface fluid solution and fluid-solid interface detection for a generic time step $\left[{}^{n}t; {}^{n+1}t\right]$ of duration Δt.

Initialization of the implicit transient dynamic scheme for the PFEM:
$k \leftarrow 0,\ \bar{\mathbf{v}}_0 \leftarrow {}^{n}\bar{\mathbf{v}},\ \bar{\boldsymbol{p}}_0 \leftarrow {}^{n}\bar{\mathbf{p}}$
while $\dfrac{\|\Delta\bar{\boldsymbol{v}}_{k+1}\|}{\|\bar{\boldsymbol{v}}_0\|}$ *and* $\dfrac{\|\bar{\boldsymbol{p}}_{k+1} - \bar{\boldsymbol{p}}_k\|}{\|\bar{\boldsymbol{p}}_0\|} >$ *tolerance* **do**
  Compute the linear momentum equations for $\Delta\bar{\mathbf{v}}_{k+1}$ (Eq. 35).
  Update the kinematics: $\bar{\boldsymbol{x}}_{k+1}, \bar{\mathbf{v}}_{k+1}, \bar{\mathbf{a}}_{k+1}$.
  Compute the continuity equation for $\bar{\boldsymbol{p}}_{k+1}$ (Eq. 38).
  $k \mathrel{+}= 1$
end
if *Mesh distortion* > *tolerance* **then**
  Erase the fluid elements and maintain the nodes (Figs. 3a and 4a).
  Create Delaunay Triangulation over the cloud of nodes (Figs. 3b and 4b).
  Do Alpha Shape check to recognize the free-surface boundaries and the fluid-solid interface (Figs. 3c and 4c).
end

4 PFEM-FEMDEM solution scheme for FSI

The FSI problem is solved by combining the FEM-DEM approach for solving non-linear solid mechanics problem (Section 2) and the PFEM to simulate the free-surface fluid flow and to detect the fluid-solid interface (Section 3.3).

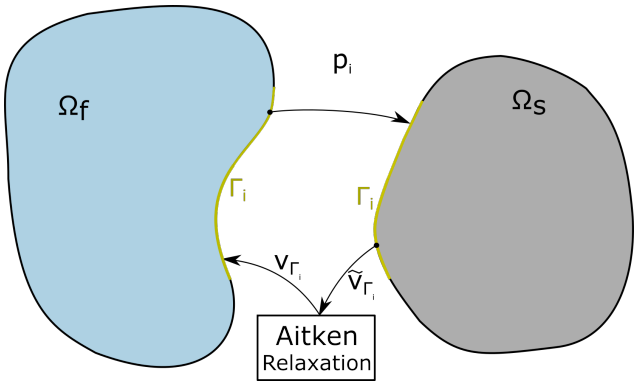

Fig. 5: Strong coupling between the fluid (Ω_f) and the solid (Ω_s) with the Aitken relaxation technique. Exchange of pressures $\mathbf{p}$ and relaxed velocities $\mathbf{v}$ at the fluid-solid interface Γ_{fs}.

The Lagrangian nature of PFEM and its efficient remeshing procedure allow for an easy transmission of boundary conditions between the fluid and the solid. Indeed, at the interface the PFEM and the FEM-DEM nodes coincide and there is no need of using any projector operator to transfer the kinematics and/or the pressures between the different domains. As the fluid-solid interface may vary during the computation, either because the fluid free-surface has changed or because some new solid contours have been formed from crack propagation, this operation must be carried out continuously during the computation (in practice at each time step). Once the new fluid mesh has been built, the FSI time step is solved maintaining as fixed the connectivity of the elements.

The solution of the coupled problem is obtained with an iterative staggered scheme. At each iteration, the fluid dynamics problem is solved implicitly with the PFEM keeping fixed the velocity at the solid boundary. The fluid pressures obtained at the interface are then transferred to the FEM-DEM as equivalent nodal forces $\mathbf{f}_{\text{fluid}}$ (Eq.(8)) and the solid mechanics solution is obtained. In case of contact between two solids, also the equivalent nodal forces due to contact $\mathbf{f}_{\text{contact}}$ of Eq. (8) are computed using the DEM particles placed at the solid boundaries (Section 2.3).

To improve the convergence and stability of the FSI scheme, an Aitken relaxation technique is adopted, analogously to [5]. A schematic representation of the algorithm is shown in Fig. 5.

Following the Aitken method, at each iteration i of the coupled problem, the velocities obtained at the fluid-solid interface Γ_{fs} from the solid FEM solution ($\tilde{\mathbf{v}}^{i+1}_{\Gamma_{fs}}$), are transferred to the fluid interface nodes as an intermediate *relaxed* velocity $\mathbf{v}^{i+1}_{\Gamma_{fs}}$, computed as:

$$\mathbf{v}^{i+1}_{\Gamma_{fs}} = \omega^{i+1}\,\tilde{\mathbf{v}}^{i+1}_{\Gamma_{fs}} + (1-\omega^{i+1})\mathbf{v}^{i}_{\Gamma_{fs}} \tag{40}$$

where the Aitken relaxation parameter ω_i is computed as:

$$\omega^{i+1} = -\omega^i \frac{\mathbf{R}^{i+1^T}(\mathbf{R}^{i+1} - \mathbf{R}^i)}{\left\|\mathbf{R}^{i+1} - \mathbf{R}^i\right\|^2} \tag{41}$$

being $\mathbf{R}^i = \tilde{\mathbf{v}}^i_{\Gamma_{fs}} - \mathbf{v}^i_{\Gamma_{fs}}$.

In this work, the initial value of the Aitken parameter has been set to 0.825.

The iterative FSI loop concludes when the following converge criterion is fulfilled:

$$\frac{\left\|\mathbf{R}^i\right\|}{\text{Number of DoF}} < tol, \tag{42}$$

Being *tol* a certain error tolerance, usually 10^{-5} m/s.

The FSI coupling method of the proposed PFEM-FEM-DEM approach is summarized in Algorithm 3.

Algorithm 3: PFEM-FEM-DEM coupled solution scheme for a time step.

For each time step:
Detect the new fluid-solid interface position with the PFEM (Section 3.3)
while $\left\|\boldsymbol{R}^i\right\| / Number\ of\ DoF > tol$ **do**
  Fix the velocity and position of the interface nodes of the solid.
  Solve the free-surface fluid flow with the PFEM (do Alg. 2)
  Free the velocities and position of the boundary nodes of the solid
  Update the values of the fluid pressure loads on the solid part (Eq. 6)
  Solve the FEM-DEM part of the calculation (do Alg. 1)
  Relax the interface nodal velocities via Aitken relaxation (Eq. 40)
  Check convergence of velocities at the interface Γ_i (Eq. 42)
end

5 Numerical examples

Five numerical examples are presented to validate the proposed PFEM-FEM-DEM formulation and to highlight specific features of the method. The first example shows the capacity of the formulation to deal with submerging solid objects in a free-surface fluid. In the second example, the accuracy of the FSI method for the solution of impacts of fluids against deformable structures is proved by analyzing a benchmark test for FSI problems in presence of free-surface fluids and large displacements of the solid structure. The same problem is then solved modifying the material parameters in order to allow the fracture and breakage of the solid. Next, the progressive collapse of a 3D solid slab due to the accumulation of a free-surface fluid is reproduced. Finally, a structural failure of a concrete wall under the action of a tsunami wave is presented.

Parameter	Value
Solid Young's modulus (E)	10 GPa
Solid Poisson's ratio (ν)	0.0
Solid Density (ρ_s)	466.07 kg/m^3
Fluid Viscosity (μ)	0.001 $Pa \cdot s$
Fluid Density (ρ_f)	1000 kg/m^3

Table 1: Wedge water entry. Material data.

5.1 Wedge water entry

This first test has been chosen to show the capability of the method to simulate the interaction between free solid debris and a free-surface fluid. A situation that may occur after the desegregation of a structure. The experimental test used as reference is the one presented in [39]. In the experiment, a solid wedge was made falling on a tank filled with water from an initial height of 1.3 m. Here, the two-dimensional adaptation of the experimental test is presented. The initial geometry of the example is depicted in Fig. 6. The material properties used are defined in Table 1. To reproduce the rigid behavior of the solid observed in the experiment, a very high value for the Young modulus of the solid has been used. The analysis has been run using a fixed time step duration of $10^{-4}s$.

The solid domain has been discretized with 5,833 3-nodded triangles whereas the fluid domain is composed of 65,586 triangles. The numerical results have been compared to the experimental observations of [39] and to the numerical results obtained by the monolithic PFEM formulation [41] and the SPH method [40].

In Fig. 7 the numerical results obtained at four different time steps are shown. The pictures show the impact of the wedge against the water at rest. The edge almost maintains the initial inclination and penetrates into the water without rotating. On the other hand, two symmetric streams of water depart laterally due to the impact of the solid object. Fig. 8 shows the time evolution of the obtained velocity of the wedge and the experimental solution. After an initial free-fall regime, the wedge decelerates progressively from a peak velocity of around 5 m/s. To better appreciate the wedge deceleration phase, Fig. 9 shows the velocity evolution of the solid after the impact against the fluid. For the same time interval, Fig. 10 also shows depict the time evolution of pressure measured at point A of the wedge.

Figs. 9-10 shows a very good agreement between the results of the proposed PFEM-FEM-DEM method and the numerical and experimental results of the literature proving the accuracy of the method in the simulation of inertially driven FSI problems.

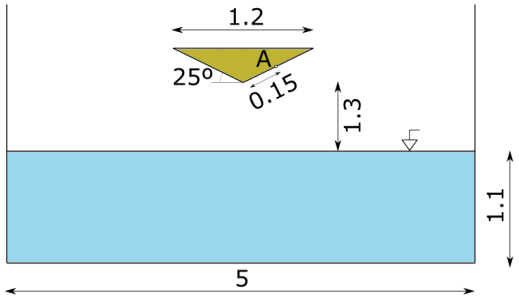

Fig. 6: Initial setup of the wedge water entry problem. Units in m.

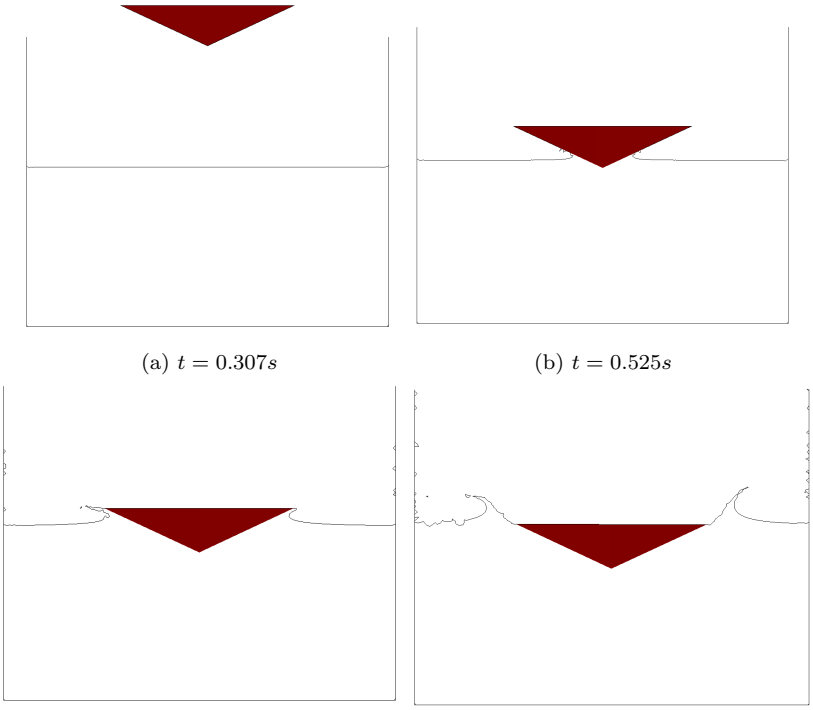

(a) $t = 0.307s$ (b) $t = 0.525s$

(c) $t = 0.590s$ (d) $t = 0.698s$

Fig. 7: Wedge water entry. Numerical results at four time instants.

5.2 Dam break against a flexible wall

The collapse of a water column against an elastic membrane is a well-known benchmark for FSI problems with free-surface fluids. The test was initially proposed by Walhorn et al. [36] and later reproduced in several other works,

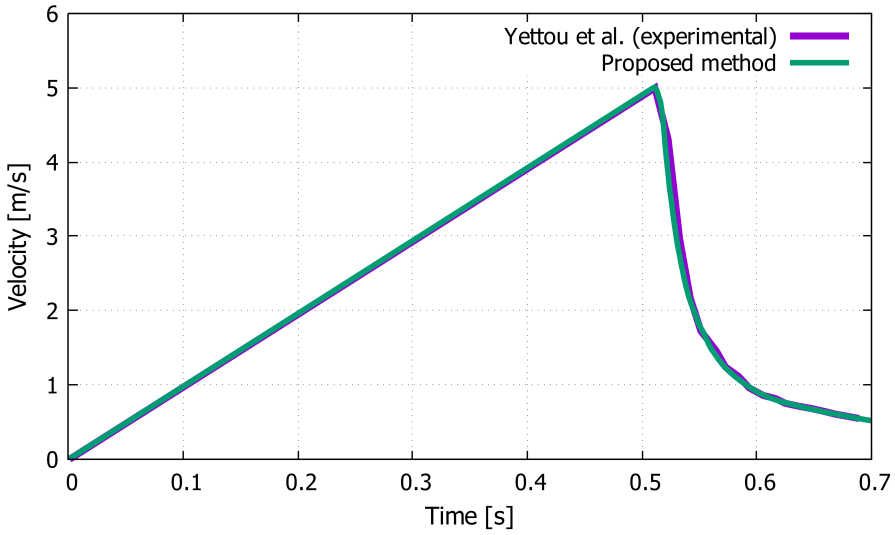

Fig. 8: Time evolution of the vertical velocity of the wedge. Comparison between the results obtained in this work and the experimental one [39].

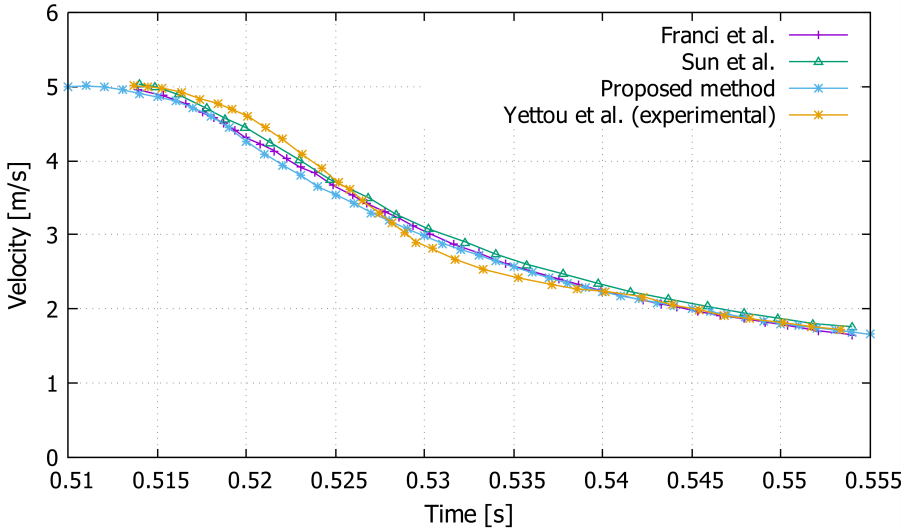

Fig. 9: Time evolution of the vertical velocity of the wedge. Comparison between the results obtained in this work and those of Sun et al. [40], Franci et al. [41] and Yettou et al. [39].

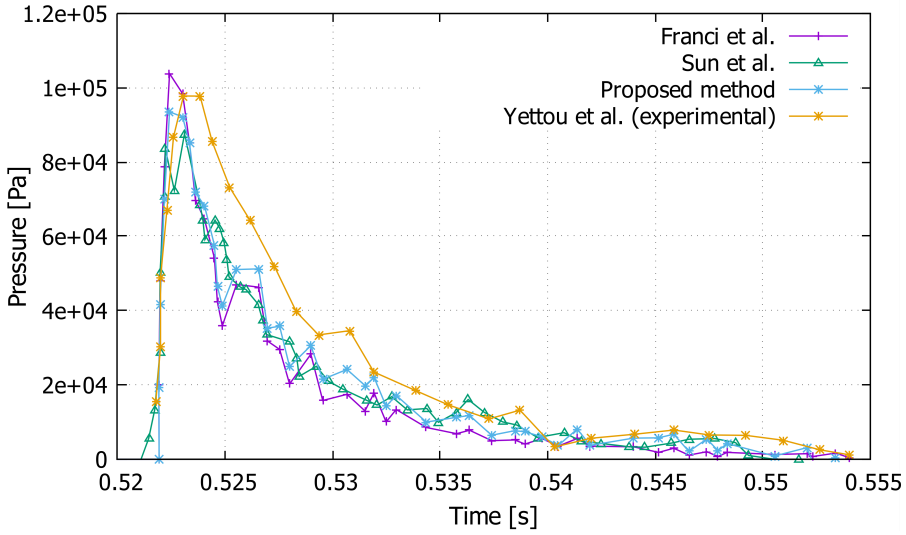

Fig. 10: Time evolution of the fluid pressure at point A of the wedge. Comparison between the results obtained in this work and those of Sun et al. [40], Franci et al. [41] and Yettou et al. [39].

some others using the PFEM [34,32,5], which are here taken as reference. The initial setup of the example is shown in Fig. 11. The material properties and the geometry data are given in Table 2. For the solid, a Neo-Hookean large strain constitutive law has been used. The initial meshes used for the solid and the fluid solutions are composed by 2,437 and 3,766 linear triangular elements, respectively.

Regarding the problem data, the time step used is Δt = 1e-3s, the relaxation procedure used is the Aitken methodology with a tolerance of 1e-5 $m/(s \cdot DoF)$ and a maximum relaxation of ω_{max} of 0.9.

The horizontal displacement of the elastic obstacle is tracked along time meanwhile is being hit by the fluid column.

Fig. 13 shows some representative snapshots of the numerical simulation.

Fig. 12 plots the time evolution of the horizontal displacement of the left top corner of the solid membrane. The graph shows an overall good agreement with the results of the literature [34,32,5].

We note that all the numerical results are almost coincident in the first 0.5s of simulation. After this time period, some discrepancy appears. Nevertheless, this can be considered as unavoidable due to the high unsteadiness exhibited by the fluid flow in this test.

Globally, the good results of this validation test confirm the suitability of the proposed method for FSI problems in presence of large displacements and deformation of both the fluid and the solid domains.

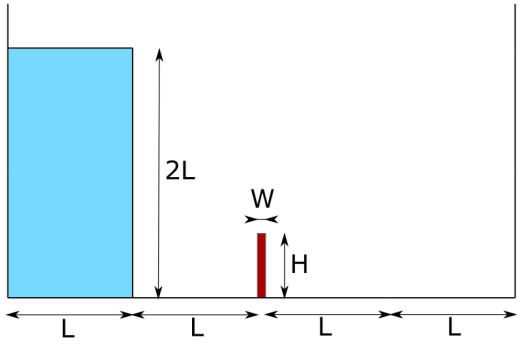

Fig. 11: Initial setup of the dam break against a flexible wall.

Parameter	Value
Solid Young's modulus (E)	1.0 MPa
Solid Poisson's ratio (ν)	0.0
Solid Density (ρ_s)	2500 kg/m^3
Solid Tensile strength (f_t)	8.0 kPa
Solid Fracture energy (G_f)	0.001 J/m^2
Fluid Viscosity (μ)	0.001 $Pa \cdot s$
Fluid Density (ρ_f)	1000 kg/m^3
L	0.146 m
H	0.080 m
W	0.012 m
Gravity	9.81 m/s^2

Table 2: Problem data for the dam break against a flexible wall.

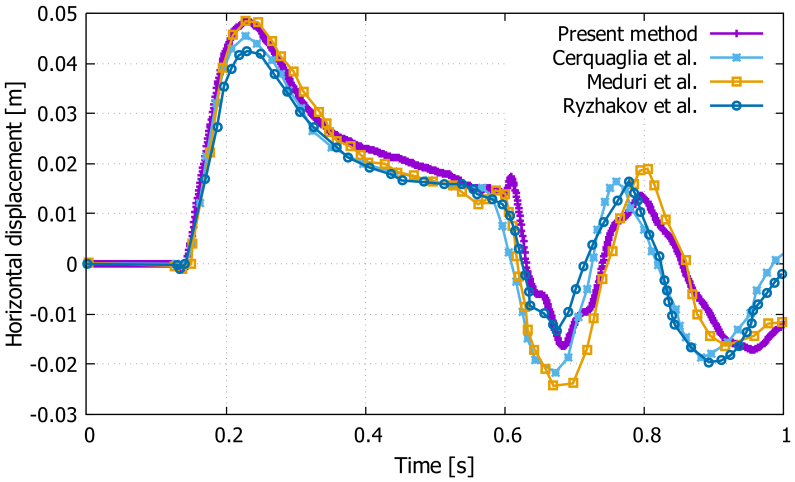

Fig. 12: Evolution of the horizontal displacement of the tip of the wall along time.

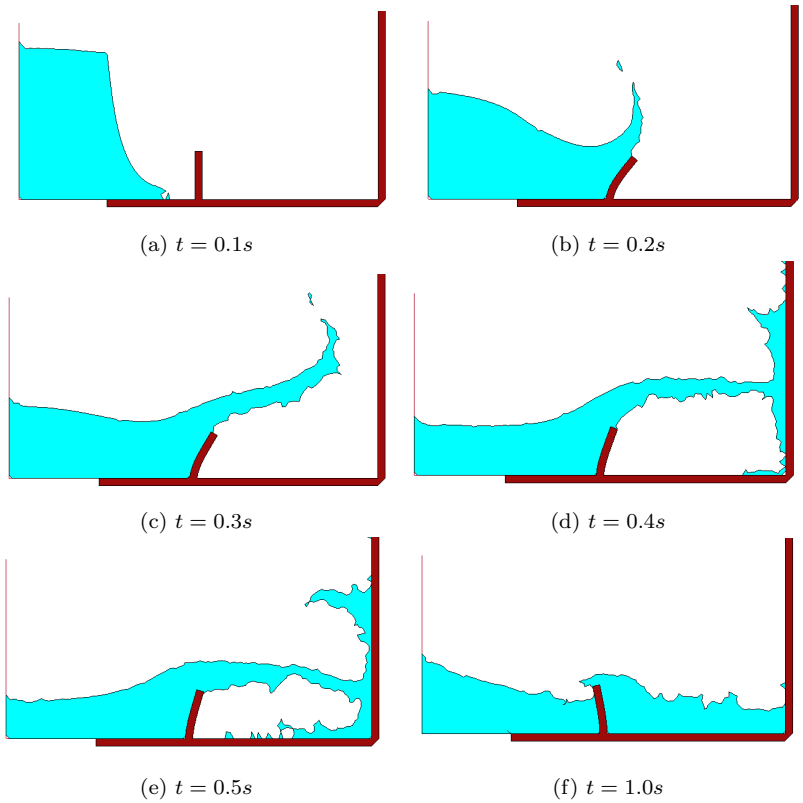

(a) $t = 0.1s$ (b) $t = 0.2s$

(c) $t = 0.3s$ (d) $t = 0.4s$

(e) $t = 0.5s$ (f) $t = 1.0s$

Fig. 13: Time lapse of the water impacting over a flexible wall.

5.3 Dam break against a fracturing wall

Here, the same test studied in Section 5.2 is analyzed changing the material properties of the solid in order to allow the breakage of the solid wall. The material properties are provided in Table 3. The solid membrane is much stiffer than the previous one and more similar to a concrete structure. An initial layer of discrete elements has been placed at the contour of the solid body to prevent the indentation between the detached wall and the ground/walls of the geometry. In this case, a lower time step was used (Δt = 1e-4s) to describe properly the violent fluid-solid and solid-solid interactions.

As shown in Fig. 14, the impact of the water on the wall induces a crack at its base. Once fully detached, the solid structure is dragged by the fluid flow and impacts against the containment walls.

Although only qualitatively, this example shows the potential of the proposed method to reproduce fracturing and breaking solids in the framework of FSI problems.

Parameter	Value
Solid Young's modulus (E)	30 GPa
Solid Poisson's ratio (ν)	0.0
Solid Density (ρ_s)	2400 kg/m^3
Yield stress (f_t)	0.5e5 Pa
Fracture energy (G_f)	10 J/m^2
Fluid Viscosity (μ)	0.001 $Pa \cdot s$
Fluid Density (ρ_f)	1000 kg/m^3
L	0.079 m
H	0.14 m
A	0.1 m
s	0.005 m

Table 3: Problem data for the dam break against a fracturing wall.

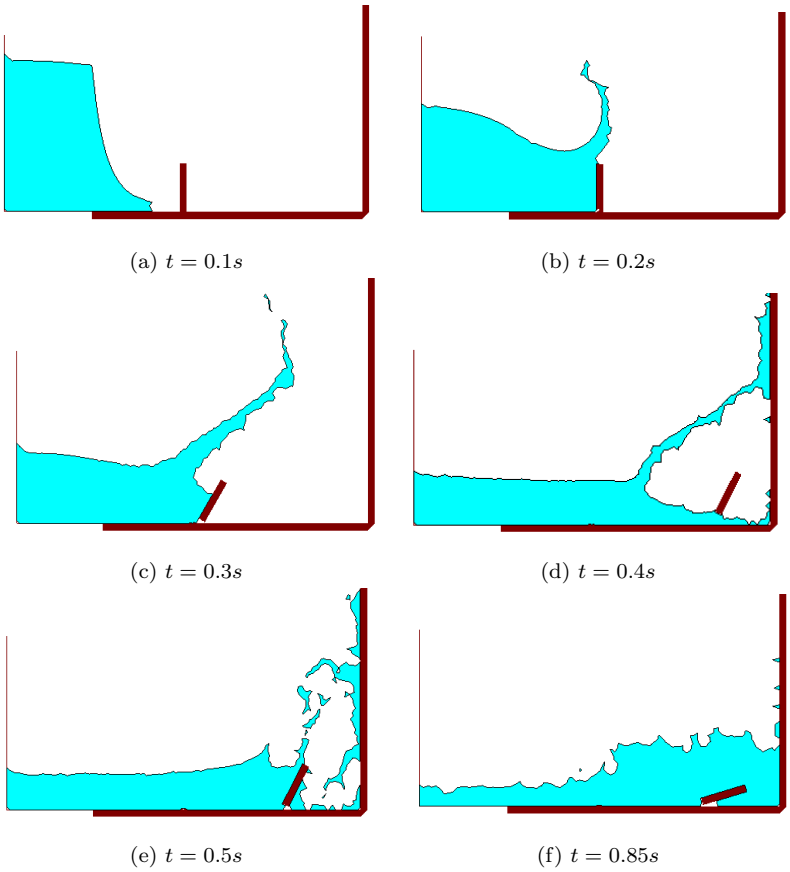

(a) $t = 0.1s$ (b) $t = 0.2s$

(c) $t = 0.3s$ (d) $t = 0.4s$

(e) $t = 0.5s$ (f) $t = 0.85s$

Fig. 14: Time evolution of the water impacting over a fracturing wall.

Parameter	Value
Solid Young's modulus (E)	35 GPa
Solid Poisson's ratio (ν)	0.2
Solid Density (ρ_s)	2400 kg/m^3
Yield stress (f_t)	0.5e6 Pa
Fracture energy (G_f)	100 J/m^2
Fluid Viscosity (μ)	100 $Pa \cdot s$
Fluid Density (ρ_f)	2400 kg/m^3

Table 4: Problem data for the 3D slab collapse example.

5.4 3D slab collapse due to fluid weight

The present example consists of simulating the failure of a slab with a central notch due to the weight of a fluid flow that accumulates on top of it. The inlet used for the fluid is inclined 45 degrees and has been positioned in the middle of the slab section (in $z-y$ plane) in order to recreate a full three-dimensional problem. The inlet lower edge is located at 0.86 m above the slab upper level. The solid slab has an initial imperfection -an artificial notch with 0.1 m height- that will propitiate the onset of the crack at the central part of the structure. The slab is fixed in the upper axis that are aligned with the initial notch.

The geometry of the problem is depicted in Fig. 15. The material properties used for the solid and the fluid domains are given in Table. 4. The yield surface used in the solid part is Rankine. The fluid is assumed to be Newtonian but very viscous and dense. The time step used ranges between $\Delta t = 10^{-3}$-10^{-4}s depending on the stage of the calculation. The Aitken velocity tolerance is $10^{-5}\ m/(s \cdot DoF)$.

Fig. 16 shows the time evolution of the collapse of the concrete slab. As can be seen, the fluid initially fills the containment of the top of the concrete slab until the maximum strength capacity of the solid is reached (around $t \approx 1.9$ s). Then, the crack is generated at the central notch ($t \approx 2$ s). Once the fracture has propagated upwards the thickness of the solid slab, the two kinematically independent bodies can rotate around its z axis aligned edges allowing the fluid to flow downwards due to gravity. The final number of finite elements used for the fluid part is 52,738 linear tetrahedra.

5.5 Failure of a concrete wall due to a tsunami force

The following numerical example attempts to reproduce the failure of a concrete structure subjected to a tsunami impulse loading. This problem was inspired by the experimental approach conducted by Arikawa et al. [66]. The geometry of the wall and its material parameters (Table 5) have been obtained from [66].

Since the length and complexity of the physical model is unfeasible in terms of computational cost, a reduced model has been studied. The generated model

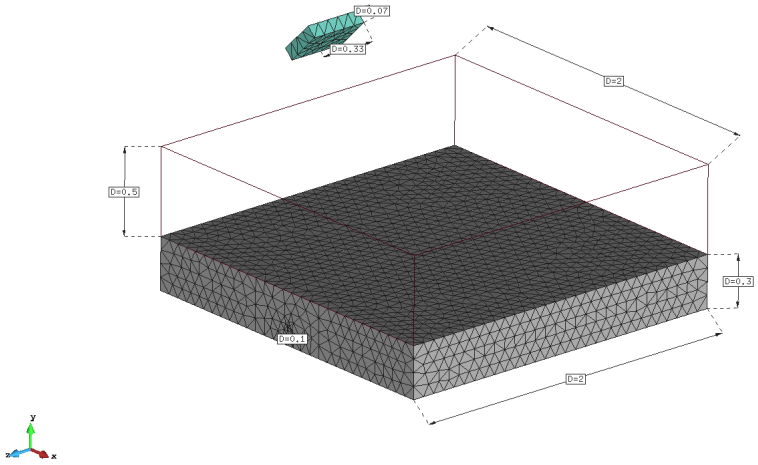

(a) Dimensions [m]

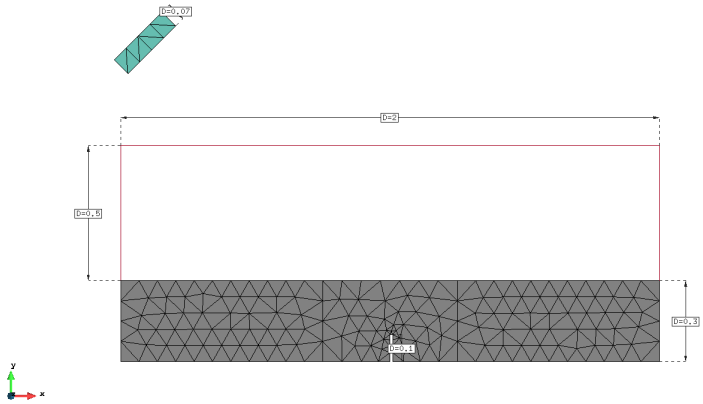

(b) FE mesh. Solid: 35,690 FE, Fluid: 153 FE.

Fig. 15: Initial geometry of the problem.

and the initial fe mesh can be seen in Fig. 17. In this figure one can perceive an initial volume of fluid on the right side of the picture. This volume has an initial velocity of 2 m/s towards the wall. Hereinafter, a constant volume of water is added to the model by an inlet, which adds fluid with an initial velocity of 2 m/s.

An adaptive time step has been used, ranging from $\Delta t = 2 \cdot 10^{-3} s$ to $\Delta t = 10^{-4} s$, in order to better capture the cracking of the wall whereas reducing the computational cost. The velocity tolerance used for the Aitken relaxation is $10^{-4}\ m/(s \cdot DoF)$.

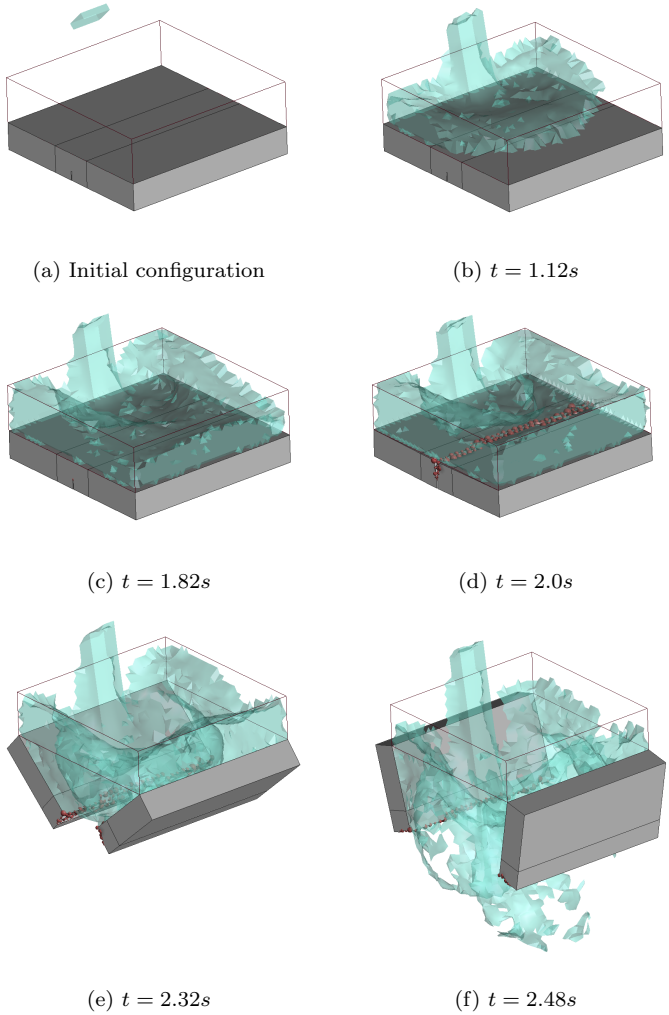

(a) Initial configuration (b) $t = 1.12s$

(c) $t = 1.82s$ (d) $t = 2.0s$

(e) $t = 2.32s$ (f) $t = 2.48s$

Fig. 16: Time evolution of the collapse of the structure.

Fig. 18 shows a time lapse of the evolution of the fluid wave -and the nodal velocities of the fluid as vectors- advancing through the channel until it hits the concrete wall. The impact of the fluid wave (Fig. 18.d) reaches a maximum velocity of 13 m/s. After the impact and detachment of the lower half of the wall, the fluid flow passes through the cavity generated. The same picture depicts the collapse mechanism of the wall, which is a punching-shear mode. This is in agreement with the experimental data provided by Arikawa et al. [66]. The fractured geometry of the wall obtained in the experiment is shown in Fig. 20.

Parameter	Value
Solid Young's modulus (E)	21 GPa
Solid Poisson's ratio (ν)	0.2
Solid Density (ρ_s)	2400 kg/m^3
Yield stress (f_t)	3e6 Pa
Fracture energy (G_f)	100 J/m^2
Fluid Viscosity (μ)	0.001 $Pa \cdot s$
Fluid Density (ρ_f)	1000 kg/m^3

Table 5: Problem data for the failure of a concrete wall under tsunami force.

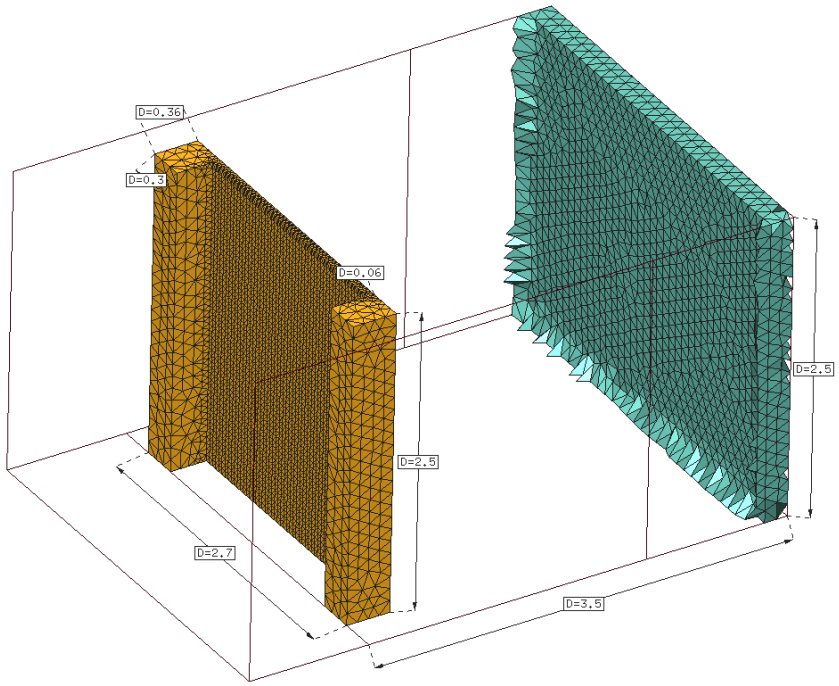

Fig. 17: Problem geometry and FE mesh. Solid: 37359 elements, Fluid: 17275 elements.

Fig. 19 shows a more detailed perspectives of the fractured geometry of the concrete wall. It is important to note that only the lower half of the wall is detached and dragged by the fluid flow, which is in agreement with the results exposed in [66].

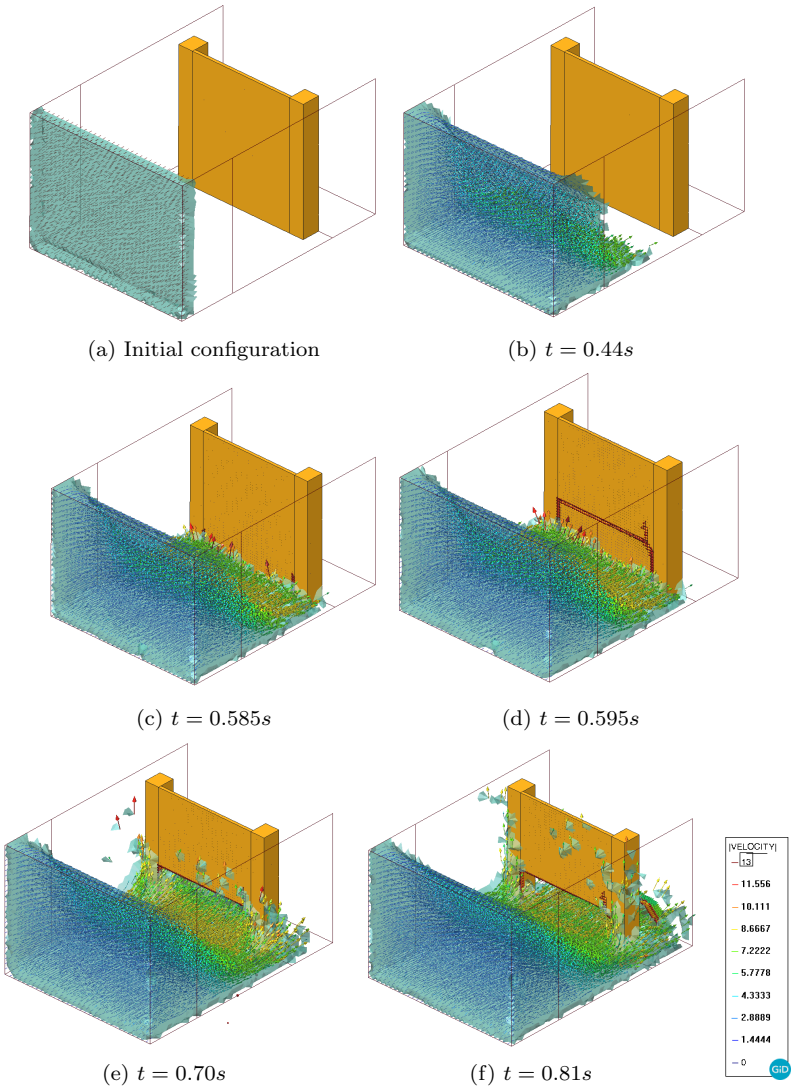

(a) Initial configuration (b) $t = 0.44s$

(c) $t = 0.585s$ (d) $t = 0.595s$

(e) $t = 0.70s$ (f) $t = 0.81s$

Fig. 18: Concrete wall under tsunami force. Velocity vectorial field of the fluid domain and cracked geometry of the structure.

6 Conclusions

We have presented a coupled Lagrangian method for the simulation of FSI problems in presence of free-surface fluids and fracturing solids.

The formulation uses the PFEM to solve the free-surface fluid dynamics problem and to detect the fluid-solid interface, and a coupled FEM-DEM method to model crack formation and propagation in structures and the con-

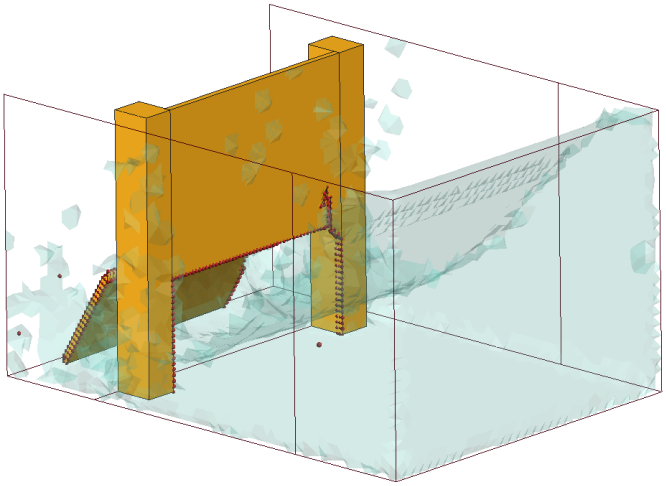

(a) Final configuration, isometric

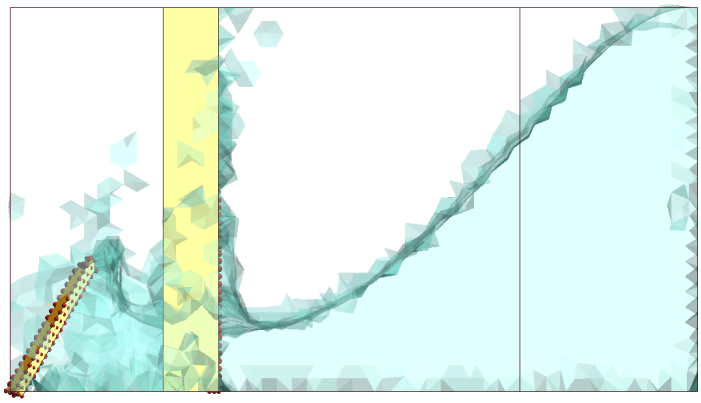

(b) Final configuration, lateral view.

Fig. 19: Concrete wall under tsunami force. Fractured geometry of the wall.

tact interaction between different solids. An iterative staggered scheme with Aitken relaxation is used to guarantee a strong coupling of the FSI problem and to avoid numerical inconveniences, such as the ill-conditioning of the linear system or added-mass effects. The numerical method presented has demonstrated to be a useful tool to estimate damages on civil constructions due to natural hazards like floods, tsunamis, landslides, or explosions.

Several academic examples have been presented to validate the proposed technology in the framework of FSI problems with fracture phenomena. The numerical tests have shown that the method is able to reproduce the dynamics of a solid object in the water, to solve accurately FSI problems with strong fluid impacts and large solid displacements, to model crack formation due to

Fig. 20: Concrete wall under tsunami force. Cracked geometry of the wall after the experiment conducted in Arikawa et al. [66].

fluid hydrodynamic forces and its propagation in the structure, and to deal with solid fragmentation and multi-body contact interaction.

A Tensors used for the FEM solution of solid mechanics problem

In this appendix, the variables and tensors introduced in Eqs. (8)-(9) are defined.

The matrices and vectors of Eq. (8) are computed as:

$$M_{KJ} = \int_{\Omega_0} \rho_0 N_{KI} N_{IJ} dV_0, \tag{43}$$

$$\mathbf{f}_{ext,K} = \int_{\partial\Omega_0} t_I N_{IK} dS_0 + \int_{\Omega_0} \rho_0 b_I N_{IK} dV_0 \tag{44}$$

$$\mathbf{f}_{int,K} = \int_{\Omega_0} S_{IJ} \bigtriangledown_I^S N_{JK} dV_0 \tag{45}$$

$$\mathbf{C} = \alpha_{\text{Ray}} \mathbf{M} + \beta_{\text{Ray}} \mathbf{K}_0 \tag{46}$$

Where N are the linear shape functions and parameters $\alpha_{\text{Ray}} = 0.5$ and $\beta_{\text{Ray}} = 0.02$ are the standard Rayleigh coefficients for obtaining the damping matrix if some damping is considered, otherwise we set these values to zero, and $\mathbf{K}_0$ is the initial stiffness matrix.

In Eq. 9, $\mathbf{K}_T(\bar{\mathbf{u}}_k)$ is the tangential stiffness matrix, whose relationship with the internal forces $\mathbf{f}_{\text{int}}$ is:

$$\mathbf{K}_T(\bar{\mathbf{u}}_k) = \frac{\partial \mathbf{f}_{\text{int}}(\bar{\mathbf{u}}_k)}{\partial(\bar{\mathbf{u}}_k)}. \tag{47}$$

In general, the tangential stiffness matrix $\mathbf{K}_T(\bar{\mathbf{u}}_k)$ depends on the tangent constitutive tensor $\boldsymbol{\mathcal{C}}_T$ whose numerical derivation can be found in [3]. This numerical procedure consists in obtaining an approximation of the tangent constitutive tensor $\boldsymbol{\mathcal{C}}_T$ by using finite differences. For the jth column of the tangent constitutive tensor (depending if one uses forward or central differences) in small strains reads:

$$\boldsymbol{\mathcal{C}}_{T,j} \simeq \frac{\boldsymbol{\sigma}(\boldsymbol{\varepsilon} + \boldsymbol{\delta\varepsilon_j}) - \boldsymbol{\sigma}(\boldsymbol{\varepsilon})}{\delta\varepsilon_j} \quad or \quad \boldsymbol{\mathcal{C}}_{T,j} \simeq \frac{\boldsymbol{\sigma}(\boldsymbol{\varepsilon} + \boldsymbol{\delta\varepsilon_j}) - \boldsymbol{\sigma}(\boldsymbol{\varepsilon} - \boldsymbol{\delta\varepsilon_j})}{2\delta\varepsilon_j} \tag{48}$$

where $\boldsymbol{\delta\varepsilon_j}$ is a zero vector except for the jth component whose value is a strain perturbation $\delta\varepsilon_j$, $\boldsymbol{\sigma}$ and $\boldsymbol{\varepsilon}$ are a measure of stresses and strains, respectively.

B FIC stabilization terms used for the PFEM solution

Here, the FIC terms used for the fluid problem stabilization and introduced in Section 3.2 are detailed. The stabilization terms of the FIC technique [9] affect the continuity equation (Eq.(38)) only.

In Eq.(38), the FIC stabilization terms $\mathbf{S}^{\tau}$ and $\mathbf{f}^{\tau}$ are computed as [9]

$$\mathbf{S}^{\tau} = \left(\frac{1}{\Delta t^2} \mathbf{M}^c + \mathbf{L} + \mathbf{M}^b \right) \tag{49}$$

$$\mathbf{f}^{\tau} = \frac{\mathbf{M}^c}{\Delta t^2} \left({}^n\bar{\mathbf{p}} + {}^n\dot{\bar{\mathbf{p}}} \Delta t \right) + \mathbf{f}^p \tag{50}$$

with

$$\begin{aligned} M^c_{IJ} &= \int_{\Omega} \tau \frac{\rho_f}{\kappa_f} N_I N_J d\Omega, \\ L_{IJ} &= \int_{\Omega} \tau (\boldsymbol{\nabla}^T N_I) \boldsymbol{\nabla} N_J d\Omega, \\ M^b_{IJ} &= \int_{\Gamma_t} \frac{2\tau}{h_n} N_I N_J, \\ f^p_I &= \int_{\Gamma_t} \tau N_I \left[\rho_f \frac{Dv_n}{Dt} - \frac{2}{h_n} (2\mu_f d_n - \hat{t}) \right] d\Gamma - \int_{\Omega} \tau \boldsymbol{\nabla}^T N_I \rho \mathbf{g} d\Omega \end{aligned} \tag{51}$$

where Γ_t is the free-surface contour and the stabilization parameter τ is defined as

$$\tau = \left(\frac{8\mu_f}{h^2} + \frac{2\rho_f}{\delta} \right)^{-1} \tag{52}$$

where h and δ are characteristic distances in space and time. Details about the derivation of the stabilization terms can be found in [9].

Acknowledgements This research was supported by the Spanish Government through the FPU 16/02697 grant and by the Spanish Ministry of Economy and Competitiveness (Ministerio de Economia y Competitividad, MINECO) through the Severo Ochoa Programme for Centres of Excellence in RD (CEX2018-000797-S) and the project PRECISE (BIA2017-83805-R). The authors gratefully acknowledge the received support.

Conflict of interest

The authors declare that they have no conflict of interest.

References

1. Zárate F. and Oñate E., A simple FEM-DEM technique for fracture prediction in materials and structures, *Computational particle mechanics*, 2, page 301-314 (2015)
2. Zárate F., Cornejo A. and Oñate E., A three-dimensional FEM–DEM technique for predicting the evolution of fracture in geomaterials and concrete, *Computational particle mechanics*, 5, 411-420 (2018)
3. Cornejo A., Mataix V., Zárate F. and Oñate E., Combination of an adaptive remeshing technique with a coupled FEM-DEM approach for analysis of crack propagation problems, *Computational particle mechanics*, 1-18 (2019)
4. Zienkiewicz OC., Zhu JZ., The superconvergent patch recovery (SPR) and adaptive finite element refinement, *Comput Methods Appl Mech Eng*, 101, 207-224 (1992)
5. Cerquaglia M.L. and Thomas D. and Boman R. and Terrapon V. and Ponthot J.P., A fully partitioned Lagrangian framework for FSI problems characterized by free surfaces, large solid deformations and displacements, and strong added-mass effects, *Comput Methods Appl Mech Eng*, 348, 409-442 (2019)
6. Franci A. and Oñate E. and Carbonell J.M., Unified Lagrangian Formulation for solid and fluid mechanics and FSI problems, *Comput Methods Appl Mech Eng*, 298, 520-547 (2016)
7. Oñate E. and Idelsohn S. and Del Pin F. and Aubry R., The Particle Finite Element Method. An overview , *International Journal of Computational Methods*, 1, 267-307 (2004)
8. Franci A. and Cremonesi M., On the effect of standard PFEM remeshing on volume conservation in free-surface fluid flow problems, *Computational particle mechanics*, 4, 331-343 (2016)
9. Oñate E. and Franci A. and Carbonell J.M., Lagrangian formulation for finite element analysis of quasi-incompressible fluids with reduced mass losses, *International Journal for Numerical Methods in Fluids*, 74, 699-731 (2014)
10. Franci A. and Oñate E. and Carbonell J.M., On the effect of the bulk tangent matrix in partitioned solution schemes for nearly incompressible fluids, *International Journal for Numerical Methods in Engineering*, 102, 257-277 (2015)
11. Edelsbrunner H. and Mucke E.P., Three dimensional alpha shapes, *ACM Trans Graphics*, 13, 43-72 (1999)
12. Edelsbrunner H. and Tan T.S., An upper bound for conforming delaunay triangulations, *Discrete and Computational Geometry*, 10, 197-213 (1993)
13. Oñate E. and Zárate F. and Miquel J. and Santasusana M. and Celigueta MA. and Arrufat F. and Gandijota R. and Valiullin K. and Ring L., A local constitutive model for the discrete element method. Application to geomaterials and concrete, *Comput Part Mech*, 2, 139-160 (2015)
14. Celigueta MA., Latorre S., Arrufat F. and Oñate E., Accurate modelling of the elastic behavior of a continuum with the Discrete Element Method, *Computational Mechanics*, 60, 997-1010 (2017)
15. Celigueta MA., Latorre S., Arrufat F. and Oñate E., An accurate nonlocal bonded discrete element method for nonlinear analysis of solids: application to concrete fracture tests, *Comp. Part. Mech*, (2019)
16. Oliver J. and Cervera M. and Oller S. and Lubliner J., Isotropic damage models and smeared crack analysis of concrete, *Second international conference on Computer Aided Analysis and Design of Concrete Structures*, (1990)
17. Casas G. and Mukherjee D. and Celigueta MA. and Zohdi TI. and Oñate E., A modular partitioned discrete element framework for industrial grain distribution systems with rotating machinery, *Computational Particle Mechanics*, 4, 181-198 (2017)
18. Thornton C. and Cummins SJ. and Cleary PW., An investigation of the comparative behaviour of alternative contact force models during inelastic collisions, *Powder Technology*, 233, 30-46 (2013)
19. Idelsohn S.R. and Oñate E. and Del Pin F., The particle finite element method: a powerful tool to solve incompressible flows with free-surfaces and breaking waves, *International Journal for Numerical Methods in Engineering*, 61, 964-989 (2004)
20. S.R. Idelsohn and J. Marti and A. Limache and E. Oñate , Unified Lagrangian Formulation For Elastic Solids And Incompressible Fluids: Applications to Fluid-Structure

Interaction Problems Via The PFEM, *Computer Methods In Applied Mechanics And Engineering*, 197, 1762-1776 (2008)
21. Ryzhakov P. and Oñate E. and Idelsohn S.R., Improving Mass Conservation in Simulation of Incompressible flows, *International Journal of Numerical Methods in Engineering*, 90, 1435-1451 (2012)
22. Oñate E., Derivation of stabilized equations for advective-diffusive transport and fluid flow problems, *Computer methods in applied mechanics and engineering*, 151, 233-267 (1998)
23. Pouplana I. and Oñate E. , A FIC based stabilized mixed finite element method with equal order interpolation for solid–pore fluid interaction problems, *International Journal for Numerical and Analytical Methods in Geomechanics*, 41, 110-134 (2017)
24. S.R. Idelsohn and N. Calvo and E. Oñate, Polyhedrization of an arbitrary point set, *Computer Methods in Applied Mechanics and Engineering*, 92 (22–24), 2649-2668 (2003)
25. C. Chuan-Miao, Optimal points of the stresses for triangular linear element, *Numerical Math. J. Chinese Univ.*, 2, 12-20 (1980)
26. Levine, N., Stress Sampling Points for Linear Triangles in the Finite Element Method, *University of Reading, Department of Mathematics*, (1982)
27. GN. Hou and J. Wang and A. Layton , Numerical Methods for Fluid-Structure Interaction—A Review. *Communications in Computational Physics*, 12(2): p. 337–377 (2012)
28. CS. Peskin ,The immersed boundary method. *Acta Num.*, 11: p. 479–517 (2002)
29. M. Ariane and MH. Allouche and M. Bussone and F. Giacosa and F. Bernard and M. Barigou and A. Alexiadis, Discrete multi-physics: A mesh-free model of blood flow in flexible biological valve including solid aggregate formation, *Plose One*, 12(4):e0174795 (2017)
30. AJ. Gil and A. Arranz Carreño and J. Bonet and O. Hassan, The immersed structural potential method for haemodynamic applications, *Journal of Computational Physics*, 229 (22), 8613-8641 (2010)
31. M. Cremonesi and A. Frangi and U. Perego, A Lagrangian finite element approach for the analysis of fluid–structure interaction problems, *International Journal for Numerical Methods in Engineering*, 84 (5), 610-630 (2010)
32. S. Meduri and M. Cremonesi and U. Perego and O. Bettinotti and A. Kurkchubasche and V. Oancea, A partitioned fully explicit Lagrangian Finite Element Method for highly nonlinear Fluid-Structure-Interaction problems *International Journal for Numerical Methods in Engineering*, 113 (1), 43-64 (2017)
33. M. Zhu and MH. Scott, Direct differentiation of the quasi-incompressible fluid formulation of fluid–structure interaction using the PFEM, *Computational Particle Mechanics* 4 (3), 307-319, (2017)
34. PB. Ryzhakov and R. Rossi and SR. Idelsohn and E. Oñate, A monolithic Lagrangian approach for fluid–structure interaction problems *Computational mechanics* 46 (6), 883-899 (2010)
35. Donea J. and Huerta A., Finite element method for flow problems. Wiley edition, New York (2003)
36. E. Walhorn and A. Kölke and B. Hübner and D. Dinkler, Fluid–structure coupling within a monolithic model involving free surface flows. *Computers and Structures* 25-26, 2100-2111 (2005)
37. R. Zorrilla and R. Rossi and R. Wüchner and E. Oñate, An embedded Finite Element framework for the resolution of strongly coupled Fluid–Structure Interaction problems. Application to volumetric and membrane-like structures. *Computer Methods in Applied Mechanics and Engineering* 368, 113179 (2020)
38. M. Cremonesi and A. Franci and E. Oñate and S.R. Idelsohn, A state of the art review of the Particle Finite Element Method. *Archives of Computational Methods in Engineering* (2020)
39. E.M. Yettou and A. Desrochers and Y. Champoux, Experimental study on the water impact of a symmetrical wedge. *Fluid Dynamics Research*, 38(1), 47–66 (2006)
40. P. Sun and F. Ming and A. Zhang, Numerical simulation of inter- actions between free surface and rigid body using a robust SPH method. *Ocean Engineering* 98:32–49 (2015)
41. A. Franci, Lagrangian finite element method with nodal integration for fluid–solid interaction. *Computational Particle Mechanics* https://doi.org/10.1007/s40571-020-00338-1 (2020)

42. Y. Li and M. Asai, Fluid-rigid body interaction simulation based on a stabilized ISPH method incorporated with the impulse-based rigid body dynamics. *Transactions of the Japan Society for Computational Engineering and Science* (2018)
43. Y. Miyagawa and M. Asai, Multi-scale bridge wash out simulation during tsunami by using a particle method. *MATEC Web of Conferences* 47,02019 (2016)
44. B. Chandra and M. Asai, Verification and validation of the fluid-rigid body interaction simulation by the smoothed particle hydrodynamics method. *Proceedings of computational engineering conference JSCES 21* (2016)
45. E. Oñate and M.A. Celigueta and S.R. Idelsohn, Modeling bed erosion in free surface flows by the Particle Finite Element Method. *Acta Geotechnia* 1(4), 237–252 (2006)
46. E. Oñate and S.R. Idelsohn and M.A. Celigueta and R. Rossi, Advances in the Particle Finite Element Method for the analysis of fluid–multibody interaction and bed erosion in free surface flows. *Computer methods in applied mechanics and engineering* 197(19-20), 1777–1800 (2008)
47. Y. Dua and F. Zhoub and L. Mad and J. Zhengc and C. Xua and G. Chena, Consequence analysis of premixed flammable gas explosion occurring in pipe using a coupled fluid-structure-fracture approach. *Journal of Loss Prevention in the Process Industries* 57, 81–93 (2019)
48. V. Keima and P. Marxa and A. Nonna and S. Münstermann, Fluid-structure-interaction modeling of dynamic fracture propagation in pipelines transporting natural gases and CO2-mixtures. *International Journal of Pressure Vessels and Piping* 175, 103934 (2019)
49. H.O. Nordhagen and S. Kragset and T. Berstad and A. Morin and C. Dørum and S.T. Munkejordand, A new coupled fluid–structure modeling methodology for running ductile fracture. *Computers and Structures* 94-95, 13–21 (2012)
50. T. Rabczuk and R. Gracie and J.H. Song and T. Belytschko, Immersed particle method for fluid–structure interaction. *International Journal for Numerical Methods in Engineering* 81, 48–71 (2010)
51. K.G. Wang and P. Lea and C. Farhat, A computational framework for the simulation of high-speed multi-material fluid–structure interaction problems with dynamic fracture. *International Journal for Numerical Methods in Engineering* 104, 585–623 (2015)
52. F. Cirak and R. Deiterding and S.P. Mauchand, Large-scale fluid–structure interaction simulation of viscoplastic and fracturing thin-shells subjected to shocks and detonations. *Computers and Structures* 85, 1049–1065 (2007)
53. R. Talemi and S. Cooreman and H. Mahgerefteh and S. Martynov and S. Brown , A fully coupled fluid-structure interaction simulation of three-dimensional dynamic ductile fracture in a steel pipeline. *Theoretical and Applied Fracture Mechanics* 101, 224–235 (2019)
54. Y. Sudhakar and W.A. Wall, A strongly coupled partitioned approach for fluid-structure-fracture interaction. *International Journal for Numerical Methods in Fluids* 87, 90–108 (2018)
55. T. Wick, Coupling fluid–structure interaction with phase-field fracture. *Journal of Computational Physics* 327, 67 –96 (2016)
56. J. Adachi and E. Siebritsb and A. Peircec and J. Desrochesd, . Computer simulation of hydraulic fractures. *International Journal of Rock Mechanics and Mining Science* 44, 739-757 (2007)
57. S. Secchi and B.A. Schrefler, A method for 3-D hydraulic fracturing simulation. *International Journal of Rock Mechanics and Mining Science* 178, 245-258 (2012)
58. I De-Pouplana and E. Oñate, Finite element modelling of fracture propagation in saturated media using quasi-zero-thickness interface elements, *Computers and Geotechnics* 96, 103-117 (2018)
59. I De-Pouplana and E. Oñate, A FIC-based stabilized mixed finite element method with equal order interpolation for solid–pore fluid interaction problems. *International journal for numerical and analytical methods in geomechanics* 41, 110-134 (2017)
60. B. Irons and R.C. Tuck, A version of the Aitken accelerator for computer implementation. *International Journal for Numerical Methods in Engineering* 1, 275-277 (1969)
61. C. Antoci and M. Gallati and S. Sibilla , Numerical simulation of fluid–structure interaction by SPH. *Comput Struct* 85, 879-890 (2007)

62. B. Ren and Z. Jin and R. Gao and Y. Wang and Z. Xu , SPH-DEM Modeling of the Hydraulic Stability of 2D Blocks on a Slope. *Journal of Waterway, Port, Coastal, and Ocean Engineering* 140(6), 04014022 (2014)
63. T. Rabczuk and R. Gracieand J. Song and T. Belytschko. Immersed particle method for fluid-structure interaction. *Int J Numer Meth Eng* 22, 48 (2010)
64. T. Rabczuk and T. Belytschko, A three-dimensional large deformation meshfree method for arbitrary evolving cracks. *Comput Methods Appl Mech Eng* 196,2777–99 (2007)
65. K. Han and YT. Feng and DRJ. Owen. Numerical simulations of irregular particle transport in turbulent flows using coupled LBM-DEM. *Comp Model Eng Sci* 18, 87 (2007)
66. T. Arikawa and K. Shimosako and N. Ishikawa. Structural failure by impulsive force. *5th International Conference on Protection of Structures against Hazards* (2012)